Yang, H., Quigley, M., and King, T., 2020, Surface slip distributions and geometric complexity of intraplate reverse-faulting earthquakes: GSA Bulletin, https://doi.org/10.1130/B35809.1.

Supplemental Material

Table 1. Published data for each event used in this manuscript

Table 2. Summary of preferred best fit models

Table 3. Description of the five models used to test the effects of depth and dip estimates on width and stress drop estimates

Table 4. Description of hypocentre OR centroid moment tensor OR modelled depths used for each model. In some cases (blue text) direct estimates for fault width were used. Models A & B use a variety of data, Models C & D use hypocentral depths (except where no reliable hypocentre data are published)

Table 5. Width results from Models A – D and Model E (Avg.) including L:W ratios, area, and average slip per area. Orange width values are direct from publications (Table 4) and not calculated using depth and dip. Green cells indicate width values used in our manuscript

Table 6. Stress drop results for Models A – D, and Model E (avg.) for four different stress drop calculations

Table 7. Various categorisations of data presented in our manuscript relative to the Type definitions 1, 2 and 3. Note that Types are defined predominately on how the geometric complexity of structures in the local bedrock (as proxied by geophysical analysis and surface geology) relates to the direction of regional S_{Hmax} (Rajabi et al., 2017).

Table 8. Cumulative sum of segment lengths per 5° increment of segment azimuth, where 0° is S_{HMax} perpendicular and 90° is S_{HMax} parallel. I.e. Faults with total lengths close to 0° are more optimally aligned for reverse failure relative to S_{HMax}. Input data for these calculations are presented in Table 10.

Table 9. Summary of the orientation of segments relative to S_{Hmax} for each Type.

Table 10. S_{Hmax} direction, and segment length and azimuth data for each earthquake

Figure 1. Comparison of the results from the 'Mean' stress drop (an average of 'Moment', '20 GPa', '50 GPa', and 'Published' across Models A – D, and Model E (which averages the widths from Models A – E).

Figure 2. Comparison of Width and L:W derived for Models A – E (Table 5)

Figure 3. Maps of fault segments as defined in Table 6 of King et al., 2019 (except Pukatja and Calingiri) with lengths and azimuthal bearings (between 000° – 180°). In some cases total lengths differ from those used in this manuscript (see Table 10). The number of segments defined for Pukatja and Calingiri differ from Table 6 of King et al., 2019 to better capture the azimuthal changes within those surface ruptures. Azimuths are calculated from end to end of each line shown.

Table 1. Published data for each event used in this manuscript

Event	Mw[1]	Length [km][2]	Avg. net-slip (AD) [m][3]	Max. net-slip (MD) [m][4]	AD:MD	Pub. Stress drop [MPa]	Stress drop reference	% DC[5]	% DC Reference
Meckering	6.6	39	1.67	3.7	0.49	9.0	(Denham et al., 1980)	66	(Vogfjord and Langston, 1987)
Calingiri	5.0	4.0	0.31	1.3	0.27	9.0	(Denham et al., 1980)		
Cadoux	6.1	23	0.47	1.8	0.28	2.0	(Denham et al., 1987)	94	USGS[6]
Marryat Creek	5.7	14	0.31	1.1	0.27			98	USGS[6]
Kunayungku	6.3	9.2	0.58	1.4	0.43	5.8	(Choy and Bowman, 1990)	79	(Choy and Bowman, 1990)
LSW	6.4	8.3	1.08	2.3	0.43	13.0	(Choy and Bowman, 1990)	40	(Choy and Bowman, 1990)
LSE	6.6	17.2	1.15	3.6	0.33	8.6	(Choy and Bowman, 1990)	100	(Choy and Bowman, 1990)
Katanning	4.7	2.5	0.17	0.3	0.67	20.5 (14-27)	(Dawson et al., 2008)		
Pukatja	5.2	1.6	0.26	1.0	0.25			98	USGS[6]
Petermann	6.1	22	0.35	1.9	0.13	2.2	(Attanayake et al., 2020)	88	USGS[6]
Lake Muir	5.3	7.1	0.28	0.75	0.38			95	USGS[6]

[1] Magnitude values from (Allen et al., 2018), Lake Muir from (D. J. Clark et al., 2020); [2] Length values from this paper; [3] Average net slip values from this paper (these vary from (King et al., 2019) as they include interpolated data points as described in the manuscript); [4] Maximum net-slip values from (King et al., 2019) and references therein, Lake Muir from (D. J. Clark et al., 2020) [5] percent double couple of focal mechanisms [6]%DC is documented for these events in a .out file from the online USGS earthquake database, accessed on 20/10/2020

Table 2. Summary of preferred best fit models

Event	Preferred best fit				Rup. Dir.	Taper (10^{-4})	Loc. of *MD*	S-transform analysis of slip residuals		
	Form	R^2	RMSE	Sym.				Dominant spatial frequency	Loc. of high-freq. *MD* (km)	Structure for spikes
Meckering	Triangle	0.75	0.27	Sym.	Bilateral.	- /1.4	Bend/Intersection	1, 2	-	-
Calingiri	Ellipse	0.68	0.49	Asym.	Bilateral	11.9 / 1.9	Bend/Stepover	3	1.3 - 2.0	Bend/Stepover
Cadoux	Triangle	0.32	0.77	Asym.	Unilateral	3.2 / 4.4	Bend	1	13 - 15	Intersection
Marryat Creek	Ellipse	0.64	0.38	Sym.		1.2 / 0.7	Intersection	2, 3	4.5 - 6	Intersection
Kunayungku	Triangle	0.72	0.32	Sym.	Unilateral	2.4 / 2.6		1, 2	-	-
LSW	Ellipse (box)	0.20	0.44	Sym.	Unilateral	2.9 / 12.2		1	-	-
LSE	Ellipse (box)	0.02	0.51	Sym.	Bilateral	6.0 / 1.9	Bend	1	6 - 9	Bend
Katanning	Ellipse	0.82	0.21	Sym.	Unilateral	3.7 / 5.0		1	-	-
Pukatja	Triangle	0.62	0.62	Asym.		4.2 / 29.2	Bend/Stepover	1 - 4	-	-
Petermann	Ellipse (box)	0.18	0.70	Sym.	Bilateral	1.9 / 1.4	Stepover	1	7 - 9	Stepover
Lake Muir	Triangle	0.56	0.42	Asym.		2.8 / 1.1	Bend	2	-	-
Average		0.50±0.27	0.47±0.18			2.7 ±1.5				

Table 3. Description of the five models used to test the effects of depth and dip estimates on width and stress drop estimates

Model	Depth/width description	Dip
A	Mixture of CMT, hypocenter, modelled width	45°
B	Mixture of CMT, hypocenter, modelled width	Preferred dips from (King et al., 2019)
C	Hypocentral depths (where possible)	45°
D	Hypocentral depths (where possible)	Preferred dips from (King et al., 2019)
E	Average width derived from Models A – E	

Table 4. Description of hypocenter OR centroid moment tensor OR modeled depths used for each model. In some cases (blue text) direct estimates for fault width were used. Models A and B use a variety of data, Models C and D use hypocentral depths (except where no reliable hypocenter data are published)

Event	Model A and B			Model C and D		
	Depth (Width) [km]	**Detail**	**REF.**	**Depth (Width) [km]**	**Detail**	**REF.**
Meckering	10	Width of fault based on balancing seismic moment, length (37 km), and dip of 37°	(Vogfjord and Langston, 1987)	7	Hypocentre from local instrument network	(Everingham, 1968)
Calingiri	1	Hypocentre from 29 local instrumental records	(~~P J~~ Gregson, 1971)	1	Hypocentre from 29 instrumental records	(~~P J~~ Gregson, 1971)
Cadoux	3	Unknown – assumed hypocentre	Geoscience Australia online earthquake catalogue	6	Hypocentre from teleseismic (?) data	(Denham et al., 1987)
Marryat Creek	3	Centroid Moment Tensor (CMT) depth (i.e. not 'initiation' depth)	(Fredrich et al., 1988)	5	Hypocentre from local instrument network	(~~Peter J~~ Gregson and Moiler, 1990)
Kunayungku	10	Fault width estimated from modelled fault fit to surface offsets measured by repeat surveying	(Bowman, 1991)	6.5	Hypocentre from local and teleseismic broadband data	(Choy and Bowman, 1990)
LSW	12			3.5		
LSE	16			4.5		
Katanning	0.9	Bottom of the fault from InSAR inversion (pure thrust model)	(Dawson et al., 2008)	1	Fault width from InSAR inversion (pure thrust model)	(Dawson et al., 2008)
Pukatja	4	CMT Depth	(~~D.~~ Clark et al., 2014)	4	CMT – same as Model A and B	
Petermann	**4**	Fault width estimate from CMT model and InSAR inversion	(Hejrani and Tkalčić, 2018; Polcari et al., 2018)	4	Fault width – same as Model A and B	
Lake Muir	1.7	Hypocentre depth from Geoscience Australia	(~~D. J.~~ Clark et al., 2020)	1.7	Same as Model A and B	

Table 5. Width results from Models A – D and Model E (Avg.) including L:W ratios, area, and average slip per area. Orange width values are direct from publications (**Table 4**) and not calculated using depth and dip. Green cells indicate width values used in our manuscript

	Width [km]					SRL : W					Area [km^2]					Avg. Slip (*AD*) / Area				
Event	**A**	**B**	**C**	**D**	**E**	**A**	**B**	**C**	**D**	**E**	**A**	**B**	**C**	**D**	**E**	**A**	**B**	**C**	**D**	**E**
Meckering	10.00	10.00	9.90	12.20	10.53	3.90	3.90	3.94	3.20	3.7	390	390	386	476	411	0.004	0.004	0.004	0.004	0.004
Calingiri	1.41	2.92	1.41	2.92	2.17	2.83	1.37	2.83	1.37	1.8	6	12	6	12	9	0.055	0.027	0.055	0.027	0.036
Cadoux	4.24	3.46	8.49	6.93	5.78	5.42	6.64	2.71	3.32	4.0	98	80	195	159	133	0.005	0.006	0.002	0.003	0.004
Marryat Creek	4.24	4.67	7.07	7.78	5.94	3.30	3.00	1.98	1.80	2.4	59	65	99	109	83	0.005	0.005	0.003	0.003	0.004
Kunayungku	10	10	9.19	10.11	9.83	0.9	0.9	1.00	0.91	0.9	92	92	85	93	90	0.006	0.006	0.007	0.006	0.006
LSW	12	12	4.95	4.04	8.25	0.7	0.7	1.68	2.05	1.0	100	100	41	34	68	0.011	0.011	0.026	0.032	0.016
LSE	16	16	6.36	7.85	11.55	1.1	1.1	2.70	2.19	1.5	275	275	109	135	199	0.004	0.004	0.011	0.009	0.006
Katanning	1.27	1.40	1.00	1.00	1.17	1.96	1.79	2.50	2.50	2.1	3	4	3	3	3	0.055	0.050	0.069	0.069	0.059
Pukatja	5.66	8.00	5.66	8.00	6.83	0.28	0.20	0.28	0.20	0.2	9	13	9	13	11	0.029	0.020	0.029	0.020	0.024
Petermann	4.00	4.00	4.00	4.00	4.00	5.50	5.50	5.50	5.50	5.5	88	88	88	88	88	0.004	0.004	0.004	0.004	0.004
Lake Muir	2.40	2.22	2.40	2.22	2.31	2.95	3.20	2.95	3.20	3.1	17	16	17	16	16	0.017	0.018	0.017	0.018	0.017

Table 6. Stress drop results for Models A – D, and Model E (avg.) for four different stress drop calculations

Event	Moment based[1]					20 GPa[2]					50 GPa[2]					Mean[4]				
	A	B	C	D	E	A	B	C	D	E.	A	B	C	D	E.	A	B	C	D	E[4]
Meckering	1.4	1.4	1.4	0.9	1.2	2.8	2.8	2.8	2.4	2.7	7.0	7.0	7.0	5.9	6.7	5.0	5.0	5.1	4.6	4.9 ± 3.2
Calingiri	5.6	1.7	5.6	1.7	2.7	3.9	2.5	3.9	2.5	2.9	9.8	6.2	9.8	6.2	7.3	7.1	4.8	7.1	4.8	6.0 ± 3.0
Cadoux	3.1	4.5	0.9	1.2	1.7	1.8	2.1	1.0	1.2	1.3	4.4	5.3	2.5	2.9	3.4	2.8	3.5	1.6	1.8	2.4 ± 1.3
Marryat Creek	1.4	1.1	0.6	0.5	0.8	1.3	1.2	0.9	0.8	1.0	3.1	2.9	2.2	2.0	2.4	1.9	1.7	1.2	1.1	1.5 ± 0.9
Kunayungku	3.2	3.2	4.0	3.1	3.3	1.7	1.7	1.7	1.7	1.7	4.2	4.2	4.4	4.1	4.2	3.7	3.7	4.0	3.7	3.8 ± 1.5
LSW	3.0	3.0	16.4	22.8	7.7	2.9	2.9	4.6	5.2	3.6	7.3	7.3	11.5	13.1	9.0	6.6	6.6	11.4	13.5	9.5 ± 5.9
LSE	2.7	2.7	11.5	8.1	4.3	1.9	1.9	3.3	2.8	2.2	4.8	4.8	8.2	7.0	5.6	4.5	4.5	7.9	6.6	5.9 ± 3.1
Katanning	4.4	3.7	6.5	6.5	5.0	2.7	2.6	3.2	3.2	2.9	6.8	6.4	8.0	8.0	7.2	8.6	8.3	9.6	9.6	9.0 ± 7.1
Pukatja	2.3	1.1	2.3	1.1	1.6	2.8	2.6	2.8	2.6	2.7	6.9	6.6	6.9	6.6	6.7	4.0	3.4	4.0	3.4	3.7 ± 2.3
Petermann	3.6	3.6	3.6	3.6	3.6	1.4	1.4	1.4	1.4	1.4	3.5	3.5	3.5	3.5	3.5	2.7	2.7	2.7	2.7	2.7 ± 1.0
Lake Muir	2.2	2.5	2.2	2.5	2.3	2.1	2.2	2.1	2.2	2.1	5.2	5.5	5.2	5.5	5.4	3.1	3.4	3.1	3.4	3.3 ± 1.6
Averages	3.0	2.6	5.0	4.7	3.1	2.3	2.2	2.5	2.4	2.2	5.7	5.4	6.3	5.9	5.6	4.9 ± 3.0	4.7 ± 3.0	5.6 ± 2.6	5.4 ± 2.7	4.8 ± 2.8

[1] 'Moment' stress drop is derived from the method of (Madariaga, 1977) using $\Delta\sigma = \frac{M_o}{CSW}$ where M_O is derived from M_W, C is a coefficient derived from *L* and *W* (assuming an elliptical fault plane), and *W* is width

[2] '20 GPa' and '50GPa' stress drops are derived from the method of (Griffith et al., 2009) based on (Madariaga, 1977) using $\Delta\sigma = \frac{\mu}{C^2}\frac{\Delta D}{W}$, where μ is shear modulus at either 20GPa or 50GPa, C is a coefficient derived from *L* and *W* (assuming an elliptical fault plane), *W* is width, and $\Delta D = \frac{AD}{L}$

[3] 'Mean Value' is the mean of all 'Moment', '20GPa', '50GPa', and published (Table 1) stress drop estimates. These values are reported in the main manuscript text and figures

[4] Values and standard deviation for each event are calculated from the 16 values in Models A – D for each event. Average stress drop of all events is calculated by a combined average of the 176 stress drops calculated in Models A – D, and standard deviation is calculated on the 11 average values of Model E.

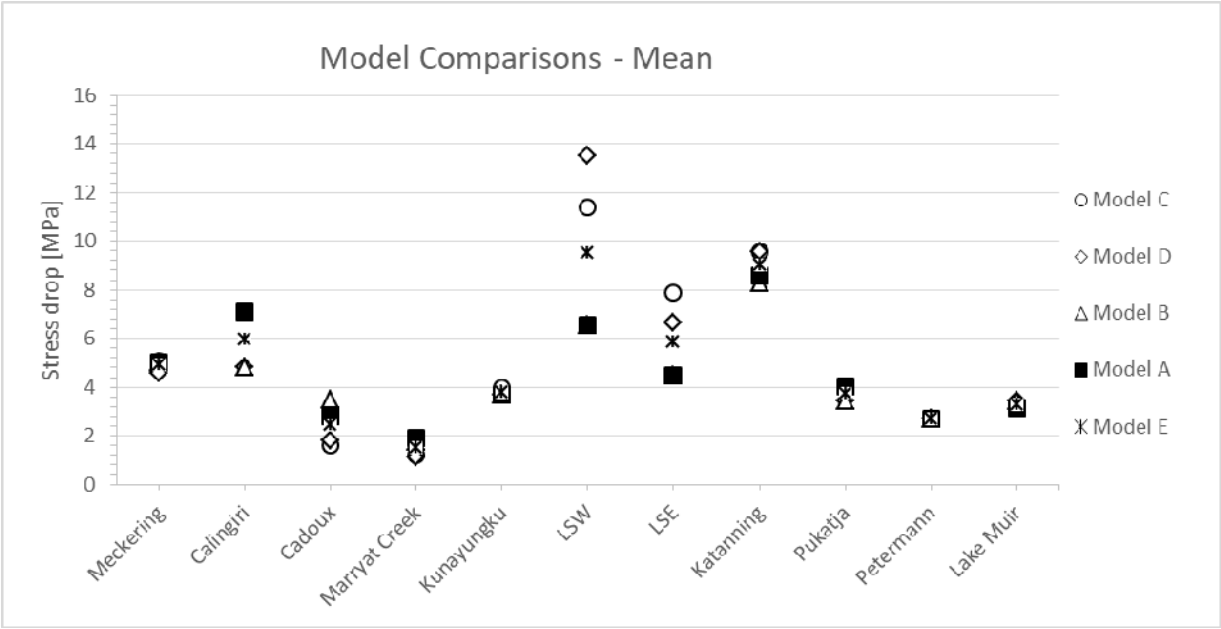

Figure 1. Comparison of the results from the 'Mean' stress drop (an average of 'Moment', '20 GPa', '50 GPa', and 'Published' across Models A – D, and Model E (which averages the widths from Models A – E).

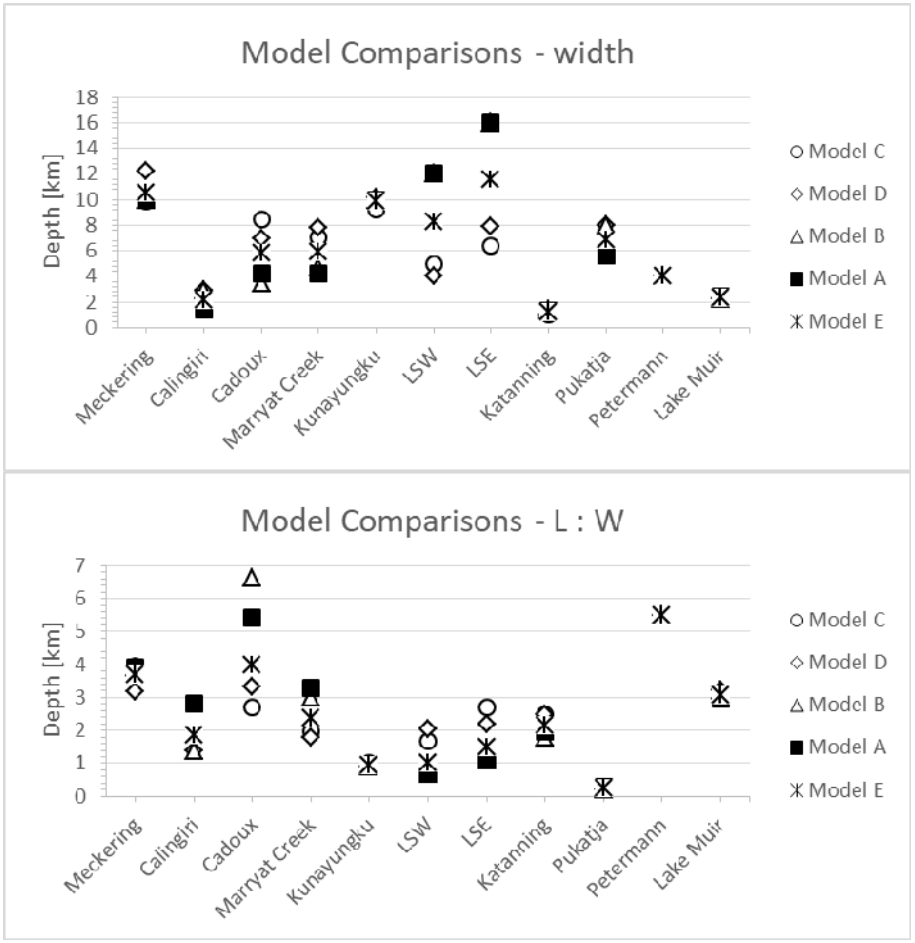

Figure 2. Comparison of Width and L:W derived for Models A – E (**Table 5**)

Table 7. Various categorisations of data presented in our manuscript relative to the Type definitions 1, 2 and 3. Note that Types are defined predominately on how the geometric complexity of structures in the local bedrock (as proxied by geophysical analysis and surface geology) relates to the direction of regional S_{Hmax} (Rajabi et al., 2017).

		Type:	**1**	**2**	**3**
		Events:	**PT, KN, LSE**	**PK, KT, MC, MCK, CL, LSW**	**LM, CD**
Rupture trace	**Straight (low geometric/kinematic complexity)**		PT, KN	CL, LSW, KT	
	Intersecting faults			MC, MCK	
	Segmented				CD?
	Multiple curved		LSE	PK	LM
Angle to S_{HMax} and gravity gradients	**Optimally orientated ~ 90°**		PT, KN, LSE	CL	LM
	Variable 0 to ± 90°			PK, KT, MC, MCK, LSW	CD
Kinematics	**Reverse**		PT, KN, LSE	CL, KT?	LM?
	Reverse + strike-slip			PK, MC, MCK, LSW	CD
Percent double couple	**High > 75%**		PT, LSE	PK, MC	LM, CD
	Moderate 40-75%		KN	LSW, MC	
	N/A			KT, CL	
Stress drop	**Low < 3.5 Mpa**		PT	MC	LM, CD
	Moderate 3.5 - 7.5 Mpa		KN, LSE	MCK, CL	
	High > 7.5 Mpa			KT, LSW	
Symmetry	**Symmetrical**		PT, KN, LSE	MCK, MC, KT	
	Asymmetrical			CL, LSW	LM, CD
Location of MD	**Middle third**		PT, KN, LSE	MCK, MC, KT, CL	LM?
	Outside middle third			LSW	CD, LM
Location of higher slip taper gradient	**Fault bend**		LSE	Cl	LM
	Step-overs		PT		
	Fault intersection			MCK, MC	CD
	N/A		KN	KT, LSW	

PT = Petermann, KN = Katanning, LSE = Lake Surprise East, PK = Pukatja, KT = Katanning, MC = Marryat Creek, MCK = Meckering, CL = Calingiri, LSW = Lake Surprise West, LM = Lake Muir, CD = Cadoux

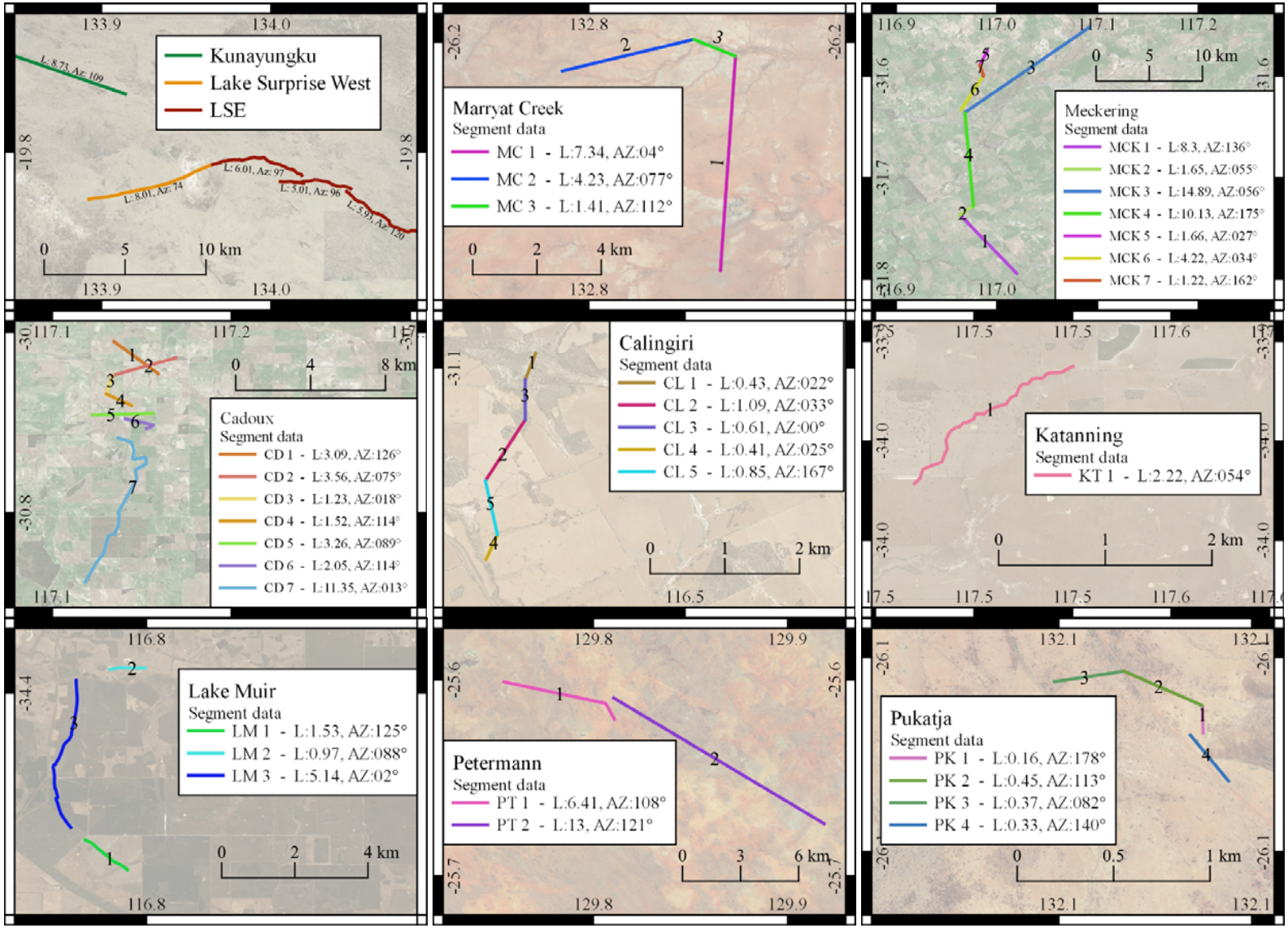

Figure 3. Maps of fault segments as defined in Table 6 of King et al., 2019 (except Pukatja and Calingiri) with lengths and azimuthal bearings (between 000° – 180°). In some cases total lengths differ from those used in this manuscript (see **Table 9**). The number of segments defined for Pukatja and Calingiri differ from Table 6 of King et al., 2019 to better capture the azimuthal changes within those surface ruptures. Azimuths are calculated from end to end of each line shown.

Table 8. Cumulative sum of segment lengths per 5° increment of segment azimuth, where 0° is S_{HMax} perpendicular and 90° is S_{HMax} parallel. I.e., Faults with total lengths close to 0° are more optimally aligned for reverse failure relative to S_{HMax}. Input data for these calculations are presented in **Table 9**.

	Cumulative percent of length per 5° bin													
Degrees	**Meckering**	**Calingiri**	**Cadoux**	**Marryat Creek**	**Kunayungku**	**LSW**	**LSE**	**Katanning**	**Pukatja**	**Petermann**	**Lake Muir**	**Type 1**	**Type 2**	**Type 3**
0 - 5	24%	18%	0%	0%	0%	0%	0%	0%	0%	0%	67%	0%	7%	34%
5 - 10	24%	18%	0%	0%	0%	0%	0%	0%	0%	0%	67%	0%	7%	34%
10 - 15	24%	43%	44%	0%	0%	0%	0%	0%	0%	0%	67%	0%	11%	55%
15 - 20	27%	43%	48%	0%	0%	0%	0%	0%	29%	0%	67%	0%	16%	58%
20 - 25	27%	68%	48%	0%	0%	0%	0%	0%	29%	0%	67%	0%	21%	58%
25 - 30	31%	68%	48%	57%	0%	0%	35%	0%	29%	0%	67%	12%	31%	58%
30 - 35	41%	100%	48%	57%	0%	0%	35%	0%	29%	67%	67%	34%	38%	58%
35 - 40	41%	100%	48%	57%	100%	0%	35%	0%	29%	67%	67%	67%	38%	58%
40 - 45	96%	100%	48%	67%	100%	0%	35%	0%	29%	67%	67%	67%	49%	58%
45 - 50	96%	100%	48%	67%	100%	0%	35%	0%	68%	100%	67%	78%	55%	58%
50 - 55	100%	100%	60%	67%	100%	0%	100%	100%	68%	100%	87%	100%	73%	74%
55 - 60	100%	100%	60%	67%	100%	0%	100%	100%	68%	100%	87%	100%	73%	74%
60 - 65	100%	100%	60%	67%	100%	0%	100%	100%	68%	100%	87%	100%	73%	74%
65 - 70	100%	100%	74%	67%	100%	0%	100%	100%	68%	100%	87%	100%	73%	81%
70 - 75	100%	100%	87%	67%	100%	100%	100%	100%	68%	100%	87%	100%	89%	87%
75 - 80	100%	100%	87%	100%	100%	100%	100%	100%	100%	100%	87%	100%	100%	87%
80 - 85	100%	100%	87%	100%	100%	100%	100%	100%	100%	100%	87%	100%	100%	87%
85 - 85	100%	100%	87%	100%	100%	100%	100%	100%	100%	100%	87%	100%	100%	87%
85 - 90	100%	100%	100%	100%	100%	100%	100%	100%	100%	100%	100%	100%	100%	100%

Table 9. Summary of the orientation of segments relative to S_{Hmax} for each Type.

	Events	Num. Events	Num. segments	Orientation of segments relative to optimal (S_{Hmax} ± 90)			
				Min.	Max	Average	St. Dev
Type 1	PT, LSE, KN	3	6	28	52	36	±18
Type 2	MCK, CL, MC, LSW, KT, PK	6	21	0	80	37	±23
Type 3	CD, LM	2	9	3	89	53	±31

Table 10. S_{Hmax} direction, and segment length and azimuth data for each earthquake

Event	SRL [km]	Sum seg. L [km][1]	S_{Hmax}[2]	S_{Hmax} ± 90	Num. of Seg.[3]	Segment length [km]							Segment azimuth [°]							Diff. to S_{Hmax} ± 90° [°]						
						1	2	3	4	5	6	7	1	2	3	4	5	6	7	1	2	3	4	5	6	7
Meckering	39	42.1	90	180	7	1.7	4.2	1.7	14.9	8.3	1.2	10.1	027	034	055	136	136	162	175	27	34	55	44	44	18	5
Calingiri	4	3.4	90	180	5	0.6	0.4	0.4	1.1	0.9			000	025	022	033	167			0	25	22	33	13		
Cadoux	23	26.1	90	180	6	11.4	1.2	3.6	3.3	1.5	2.1	3.1	013	018	075	089	114	114	126	13	18	75	89	66	66	54
Marryat Creek	14	13	67	157	3	7.3	4.2	1.4					004	77	112					27	80	45				
Kunayungku	9.2	8.7	58	148	1	8.7							109							39						
LSW	8.3	8.0	58	148	2	8.0							74							74						
LSE	17.2	17	58	148	2	5.9	5.0	6.0					120	096	097					28	52	51				
Katanning	2.5	2.2	89	179	1	2.2							054							55						
Pukatja	1.6	1.2	69	159	3	0.5	0.4	0.3					113	082	140					46	77	19				
Petermann	22	19.4	64	154	2	6.4	13.0						108	121						46	33					
Lake Muir	7.1	7.6	89	179	3	5.1	1.0	1.5					02	088	125					3	89	54				

[1] Summed lengths of segments differ slightly from the SRL lengths used elsewhere in this manuscript. SRL length of Meckering differs significantly to summed segment length as segments include the Splinter fault, which is not included in the SRL of this manuscript but is included in King et al., 2019.
[2] S_{Hmax} is derived from Rajabi et al., 2017.
[3] The number of segments comes from King et al., 2019 with the exception of Calingiri and Pukatja, were extra segmentation was added to accommodate changes in along-rupture azimuth (Fig. 3).

REFERENCES CITED

Allen, T., Leonard, M., Ghasemi, H., and Gibson, G., 2018, The 2018 National Seismic Hazard Assesment: Earthquake epicentre catalogue (GA Record 2018/30): Geoscience Australia, Commonwealth of Australia, https://doi.org/https://doi.org/10.11636/Record.2018.030.

Attanayake, J., King, T.R., Quigley, M.C., Gibson, G., Clark, D., Jones, A., and Sandiford, M., 2020, Rupture Characteristics and the Structural Control of the 2016 Mwp 6.1 Intraplate Earthquake in the Petermann Ranges, Australia: Bulletin of the Seismological Society of America, https://doi.org/10.1785/0120190266.

Bowman, J.R., 1991, Geodetic evidence for conjugate faulting during the 1988 Tennant Creek, Australia earthquake sequence: Geophysical Journal International, v. 107, no. 1, p. 47–56, https://doi.org/10.1111/j.1365-246X.1991.tb01155.x.

Choy, G.L., and Bowman, J.R., 1990, Rupture process of a multiple main shock sequence: analysis of teleseismic, local and field observations of the Tennant Creek, Australia, earthquakes of January 22, 1988: Journal of Geophysical Research, v. 95, B5, p. 6867–6882, https://doi.org/10.1029/JB095iB05p06867.

Clark, D.J., Brennand, S., Brenn, G., Garthwaite, M.C., Dimech, J., Allen, T.I., and Standen, S., 2020, Surface deformation relating to the 2018 Lake Muir earthquake sequence, southwest Western Australia: New insight into stable continental region earthquakes: Solid Earth, v. 11, no. 2, p. 691–717, https://doi.org/10.5194/se-11-691-2020.

Clark, D., McPherson, A., Allen, T., and De Kool, M., 2014, Coseismic surface deformation caused by the 23 March 2012 Mw 5.4 Ernabella (Pukatja) earthquake, central Australia: Implications for fault scaling relations in cratonic settings: Bulletin of the Seismological Society of America, v. 104, no. 1, p. 24–39, https://doi.org/10.1785/0120120361.

Dawson, J., Cummins, P.R., Tregoning, P., and Leonard, M., 2008, Shallow intraplate earthquakes in Western Australia observed by Interferometric Synthetic Aperture Radar: Journal of Geophysical Research. Solid Earth, v. 113, no. 11, p. 1–19, https://doi.org/10.1029/2008JB005807.

Denham, D., Alexander, L.G., Everingham, I.B., Gregson, P.J., McCaffrey, R., and Enever, J.R., 1987, The 1979 Cadoux earthquake and intraplate stress in Western Australia: Australian Journal of Earth Sciences, v. 34, no. 4, p. 507–521, https://doi.org/10.1080/08120098708729429.

Denham, D., Alexander, L.G., and Worotnicki, G., 1980, The stress field near the sites of the Meckering (1968) and Calingiri (1970) earthquakes, Western Australia: Tectonophysics, v. 67, p. 283–317, https://doi.org/10.1016/0040-1951(80)90271-1.

Everingham, I.B., 1968, Preliminary Report on the 14 October 1968 Earthquake at Meckering, Western Australia (BMR Record 1968/142) (1968/142): https://doi.org/http://pid.geoscience.gov.au/dataset/ga/12254.

Fredrich, J., Mccaffrey, R., and Denham, D., 1988, Source parameters of seven large Australian earthquakes determined by body waveform inversion: Geophysical Journal, v. 95, p. 1–13, https://doi.org/10.1111/j.1365-246X.1988.tb00446.x.

Gregson, P.J., 1971, Mundaring Geophysical Observatory Annual Report, 1970 (BMR Record 1971/77): Bureau of Mineral Resources, Geology and Geophysics, https://doi.org/http://pid.geoscience.gov.au/dataset/ga/12614.

Gregson, P.J., and Moiler, Y., 1990, Australian Seismological Report, 1986 (BMR Record 1990/294): Bureau of Mineral Resources, Geology and Geophysics, https://doi.org/http://pid.geoscience.gov.au/dataset/ga/15206.

Griffith, W.A., Di Toro, G., Pennacchioni, G., Pollard, D.D., and Nielsen, S., 2009, Static stress drop associated with brittle slip events on exhumed faults: Journal of Geophysical Research. Solid Earth, v. 114, no. 2, p. 1–13, https://doi.org/10.1029/2008JB005879.

Hejrani, B., and Tkalčić, H., 2018, The 20 May 2016 Petermann Ranges earthquake: centroid location, magnitude and focal mechanism from full waveform modelling: Australian Journal of Earth Sciences, v. 66, no. 1, p. 37–45, https://doi.org/10.1080/08120099.2018.1525783.

King, T.R., Quigley, M.C., and Clark, D., 2019, Surface-rupturing historical earthquakes in Australia and their environmental effects: new insights from re-analyses of observational data: Geosciences, v. 9, no. 10, p. 1–34, https://doi.org/10.3390/geosciences9100408.

Madariaga, R., 1977, Implications of stress-drop models of earthquakes for the inversion of stress drop from seismic observations: Pure and Applied Geophysics PAGEOPH, v. 115, no. 1–2, p. 301–316, https://doi.org/10.1007/BF01637111.

Polcari, M., Albano, M., Atzori, S., Bignami, C., and Stramondo, S., 2018, The Causative Fault of the 2016 Mwp 6.1 Petermann Ranges Intraplate Earthquake (Central Australia) Retrieved by C- and L-Band InSAR Data: Remote Sensing, v. 10, no. 8, p. 1311, https://doi.org/10.3390/rs10081311.

Rajabi, M., Tingay, M., Heidbach, O., Hillis, R.R., and Reynolds, S.D., 2017, The present-day stress field of Australia: Earth-Science Reviews, v. 168, no. February, p. 165–189, https://doi.org/10.1016/j.earscirev.2017.04.003.

Vogfjord, K.S., and Langston, C.A., 1987, The Meckering earthquake of 14 October 1968: A possible downward propagating rupture: Bulletin of the Seismological Society of America, v. 77, no. 5, p. 1558–1578.